

Final Year Honors Project  
for the degree of  
B.Eng(Hons) in Mechanical Engineering

## **Statistical shape modelling of femurs**

**Edwin Tay Wei Shen**

April 2020

Project Supervisor : Dr. Uwe Wolfram

Department of Mechanical Engineering  
School of Engineering and Physical Sciences  
Heriot-Watt University  
Edinburgh, United Kingdom

## 1. Abstract

In this paper, a means to generate statistical shape models of femurs from finite element meshes was investigated. Two approaches were identified, converting the finite element meshes to stereolithography meshes and working with the latter, and extracting the nodal data from the surface of the finite element meshes and working with a point cloud. In the pipeline of both approaches the dataset was aligned, registered, and principal component analysis was carried out to generate statistical shape models. The alignment step in both approaches was found to be satisfactory as evaluated by average and Hausdorff distances. The registration step however was found to be unsatisfactory when compared with existing works. Key sources of error include the 'jagged' nature of finite element meshes. The final shape models revealed that the mesh approach was able to generate a much more compact and definite statistical shape model, with the variations described by each eigenmode much clearer. Therefore, the mesh approach has been identified as the superior approach in generating statistical shape models of femurs.

# Contents

<b>1 Abstract</b>	<b>1</b>
<b>2 Introduction</b>	<b>4</b>
<b>3 Literature Review</b>	<b>5</b>
3.1 Medical Background . . . . .	5
3.2 Socio-economic Background . . . . .	6
3.3 Shape Modelling . . . . .	6
<b>4 Methodology</b>	<b>9</b>
4.1 Materials . . . . .	9
4.2 Point Distribution Models . . . . .	10
4.3 Modelling Approach . . . . .	11
4.4 Data Preparation . . . . .	12
4.4.1 Mesh Approach . . . . .	12
4.4.2 Node Approach . . . . .	13
4.5 Alignment . . . . .	13
4.6 Correspondence and PCA . . . . .	14
4.6.1 Mesh Approach . . . . .	14
4.6.2 Node Approach . . . . .	17
4.6.3 Principal Component Analysis . . . . .	17
<b>5 Results and Discussion</b>	<b>18</b>
5.1 Alignment Evaluation . . . . .	18
5.2 Registration Evaluation . . . . .	23
5.3 Model Evaluation . . . . .	25
<b>6 Conclusions and Further Work</b>	<b>29</b>

7 Acknowledgements	30
8 Appendix	35

## 2. Introduction

Osteoporosis, osteoarthritis, bone metastases, and other bone related diseases represent a significant public health concern in the modern world. With the global population aged 60 years and older estimated to be 962 million in 2017, the United Nations estimates that by 2050, the population of older persons (aged 60 and above) will outnumber the population of adolescents and youths by 0.1 billion [1]. With an ageing population, a multitude of ageing-related diseases will become more prevalent in society, contributing to significant socio-economic burdens to public healthcare systems all over the world [2]. Advances in the field of medical technology to reduce the burden on healthcare systems without sacrificing quality of patient care is of paramount importance.

In current clinical practice, osteoporosis is diagnosed by measuring bone mineral density (BMD) through the use of dual-energy X-ray absorptiometry (DXA), this is then compared with the World Health Organization's (WHO) standards [3, 4]. However, the use of BMD comparisons only explain about 30% of all osteoporotic fractures [5]. A recent study has demonstrated that the use of finite element analysis (FEA) based off three-dimensional FE models of bones can describe the variance in bone strength in up to 20% more cases than DXA models [6]. 3D patient specific bone models have further applications in orthopaedic surgery planning, teaching, research, and fabrication of customized implants and fixators [7, 8].

Current techniques in use to generate 3D models of patient specific bones utilize computed tomography (CT) imaging, however this exposes patients to unnecessarily high levels of radiation doses, potentially leading to further health problems such as cancer [9, 10]. This has been highlighted by clinical experts who warn of the excessive use of CT imaging in current medical practice [11]. Furthermore, CT imaging is expensive compared to DXA, and not as widespread in rural areas of high-income countries and in most areas of many low and middle-income countries due to the lack of necessary equipment [9, 12].

A solution to this dilemma is the use of *statistical models of shape and appearance (SSAMs)*. SSAMs are statistical models which are able to describe the mean shape and principal modes of variation of a dataset [13, 14]. The creation of a SSM will be investigated using an input dataset of finite element (FE) femur meshes. The created SSM will then have further applications in creating an SSAM for use in predicting both patient specific shape and bone density from a single 2D DXA image of a femur. The output from this project will have a direct and positive impact on the diagnosis and treatment of osteoporosis, osteoarthritis, and other bone-related diseases. This simplification in generation of patient-specific 3D models would allow for personalised fracture risk assessments and advanced personalised treatment strategies, such as personalised implants, all at lower financial and personnel costs to the medical profession.

### 3. Literature Review

#### 3.1. Medical Background

Osteoporosis is the most common chronic metabolic bone disease experienced by humans [15]. It is characterised by the gradual reduction of bone mass, degradation of bone tissue, and disruption of the inner trabecular bone structure [15, 16]. This is more succinctly described by a progressive decrease in BMD [17]. A decrease in BMD leads to a significantly higher risk of fractures, termed osteoporotic or fragility fractures [17, 18]. A dated projection from 1992 estimates that more than 200 million people worldwide suffer from osteoporosis [19], and the International Osteoporosis Foundation (IOF) estimates that 3.5 million people in the UK currently live with osteoporosis [20]. Regular and effective monitoring in high-risk individuals allows for extra care and awareness to be taken by patients to reduce risks of falls and fractures [15]. The current means of diagnosis and monitoring include obtaining a T-score from a patient's BMD which is then compared with WHO standards [15, 18]. Another means of monitoring is the use of the WHO's Fracture Risk Assessment Tool (FRAX) which is a web-based algorithm which outputs a fracture risk probability based on user input risk factors [18, 17]. However, these methods are risk-factor based and do not base on proper engineering deduction and reasoning. Cody et al. demonstrates the increased effectiveness of evaluating bone strength through patient-specific FEA [6].

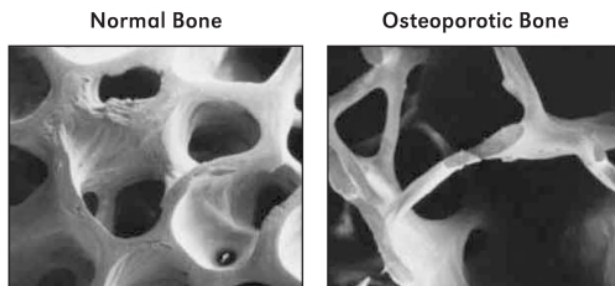


Figure 1: Comparison of normal (left) vs osteoporotic (right) bone structure [21]

Osteoarthritis is defined as a *common complex disorder with multiple risk factors*. Both genotype and phenotype constitute risk factors in developing osteoarthritis. Examples of risk factors include genetics, constitution (age, sex, obesity), and biomechanical (joint injury, occupational/recreational usage) [22]. These factors lead to focal damage and loss of articular cartilage, abnormal remodelling and attrition of subarticular bone, and osteophytes [23, 24]. The symptoms of this disorder are mild to severe joint pain and stiffness; osteoarthritis has been described as the most common joint disorder in the world and a recurring cause for loss of function and disability in adults [23, 24]. It is estimated that worldwide, 9.6% of men and 18% of women exhibit symptomatic osteoarthritis [25]. There are more drastic means of treatment for severe cases of osteoarthritis, namely prosthetic implant arthroplasty [26]. In cases of patellofemoral osteoarthritis, the use of arthroplasty as a treatment has seen widespread success due to improvements in implant design [27]. A crucial component of arthroplasty is accurate 3D models and reconstructions of patient-specific regions

of interest, which assist greatly in planning of surgical procedures and the design of implants [28].

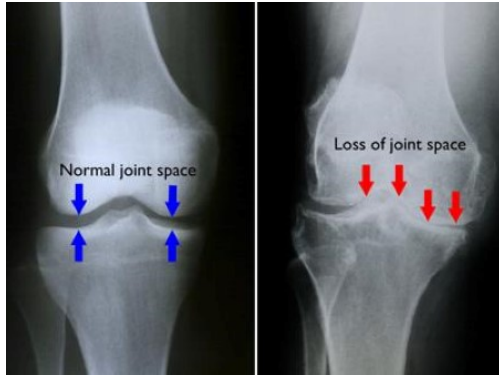


Figure 2: Comparison of normal (left) vs osteoarthritic (right) knee [29]

### 3.2. Socio-economic Background

According to the Office of National Statistics, the total healthcare expenditure by the UK government amounted to £197.4 billion in 2017, which accounted for 9.6% of the gross domestic product(GDP) [30]. Similarly across the European Union, the EU-28 countries spend an average of 9.9% of GDP on healthcare with the highest proportion of spending being 11.5% by France, roughly €260 billion (£220 billion) [31]. The possibility of alleviating the financial burdens for countries with publicly funded healthcare systems would benefit a country's overall economy and allow surplus funds to be directed towards other socio-economic concerns.

A measure of the social impact of chronic diseases can be in terms of the loss of quality-adjusted life years (QALYs). A QALY can be loosely defined as a measure of the 'quality' years left in a person's life post-treatment of a medical condition; one QALY is equal to one year of life in perfect health [32]. In the UK, the IOF estimates that roughly 183,000 QALYs were lost in 2017 due to fragility-related fractures, with similar or higher losses across other EU6 countries [20]. The potential for chronic bone diseases to lead towards further mental health issues due to the loss of independence is a significant social factor [33]. The possibility of early diagnosis, treatment, and prevention of fragility related fractures and other bone associated diseases will benefit societies greatly.

### 3.3. Shape Modelling

A comprehensive review of existing literature and latest developments within the field of statistical shape modelling was carried out by Heimann and Meinzer [14]. They summarised the variety of approaches to creating SSMs in current use and these will be briefly discussed. Deformable models based on *snakes*, an energy minimizing-spline algorithm coined by Kass et al. [34] for 2D shapes and developed further for

3D shapes by the same group [35] have found widespread use in the field of image segmentation and 3D shape generation. An extensive survey of deformable surface methods is carried out by Montagnat et al. [36]. However, as noted by Heimann, stabilizing energies that snakes are based on generally account for smoothness properties rather than statistical data [14]. Level-sets developed by Osher and Sethian [37] and applied to shape modelling by Malladi et al. [38] are also an approach. Saito et al. demonstrated this approach in creating multi-shape statistical shape models of nested structures, specifically applied to brain and ventricle volumes of human embryos [39]. Level-sets are an implicit representation of surface points, in comparison to more popular discrete representations such as meshes [36]. Shape modelling has found extensive use in a variety of fields such as archaeological research [40], biological anthropology [41], psychology [42], and biomedical engineering [14, 43].

The seminal works of Cootes and Taylor were highly influential towards the modern field of shape and appearance modelling. In their publication from 1995 they coined the term *Point Distribution Models* (PDMs) which refer to SSAMs constructed from an input dataset by calculating the mean position and variance of common points, hereby referred to as landmarks, across a dataset [44]. They illustrated this concept with an example of resistors; by defining resistors of varying shapes and sizes as a fixed number of interconnected and anatomically significant landmarks, the mean location and variance of each point can be calculated and therefore a mean shape can be generated alongside modes of variation obtained from a principal component analysis (PCA). In the same paper, they described the creation of Active Shape Models (ASMs) whereby SSMs are utilized in object identification and location. In another publication, they described a method to generate SAMs, which model texture variation alongside shape variation, where texture in this instance refers to gray levels [45]. They also later demonstrated the applicability of their approach in image registration and segmentation of medical imaging [13].

The PDM approach has gained traction and is widely utilised within the shape modelling community. Benjelloun et al. utilised an active shape model approach to develop a framework for vertebra segmentation [46]. Similarly, Rajamani et al. developed a PDM-based SSM for use in surface reconstruction from sparse data [47]. Thodberg and Rosholt also demonstrated an applicability of PDMs in the development of a novel medical device for use in bone densitometry [48]. A comprehensive review by Sarkalkan et al. discusses many other examples of PDM applications in the biomedical field, specifically in modelling bones [43]. Fitzpatrick et al. utilised SSMs to quantify the relationship between the geometry and performance of patellofemoral joints [49]. Articulated SSMs (aSSMs) are of note as well as first proposed by Heap and Hogg [50]. They postulated representing subsets of points as polar coordinates to capture rotational variability, allowing for the accounting of neighboring anatomical structures. Balestra et al. demonstrated this by creating an aSSM of a hip joint which accounted for both the pelvis and the femur [51]. Similarly, Kainmueller et al. created a similar model, albeit for segmentation purposes [52].

The pipeline of shape modelling consists of three main steps, namely alignment, registration, and PCA. Alignment is necessary as input shapes to a dataset could be in varying placements and orientations which do not factor in to the shape variation itself [53]. The alignment problem can be solved by Procrustes

Alignment [54, 55] as demonstrated by Humbert et al. [56]. Umeya formulated this as a least-squares estimation between point patterns [57] and applied by Lüthi et al. [58]. An iterative closest points (ICP) method could also be applied, similar to the least-squares estimation but formulated as a recursive function [59]. This was demonstrated by Vos et al. [60]. Generalized Procrustes Analysis (GPA) is a similar method [61, 62] which incorporates reselction of reference shape based on a mean of the dataset [46].

The registration/correspondence problem is an active research field within the shape modelling community. In the case of manually defined landmarks, correspondence across a dataset is inherent and can be considered the 'gold standard' [61]. However, in the case of complex three dimensional structures, manual landmarking is tedious and time consuming, therefore optimal automatic registration methods are necessary. Tam et al. conducted an extensive review within the general field of point cloud registration [63]. A minimum description length optimisation framework has been proposed in the past [64, 65] and has been applied by Rajamani et al. [47]. The deformable mesh method, wherein a deformable template mesh is created and utilized to generate the dataset meshes based off CT imaging is also a valid means of establishing correspondence [66]. This has been applied extensively to bone-based shape models [67, 68]. The Gaussian Process Morphable Model (GPMM) approach proposed by Lüthi et al. significantly extends the flexibility of shape models through the possibility of modelling utilising synthetically defined kernels (an alternate term for covariance function) [58]. The GPMM approach can be utilised for non-rigid registration as well as demonstrated by Chandran et al. [69]. Variations of the ICP algorithm can also be applied for registration purposes [63, 68, 70, 71].

Algorithms for SSM generation can be implemented in any programming language, however there are existing softwares which streamline the process. An approach to solving the registration problem alongside shape model generation integrated within an open-source software has been developed at the University of Utah named ShapeWorks [72]. They propose a novel approach to SSM development termed Particle Based Modeling (PDM) and this has been demonstrated in several studies [73, 74, 75]. However, this software is relatively new and unstable, and also relies on very specific data types as input files. The Graphics and Vision Research Group based in the University of Basel have developed a library of tools for shape modelling and analysis implemented in the Scala language called Scalismo [58]<sup>1</sup>. The use of a library of tools rather than methodology-specific software allows for an additional degree of flexibility in terms of customisation towards study-specific eccentricities.

---

<sup>1</sup><https://scalismo.org/>

## 4. Methodology

### 4.1. Materials

A dataset of 77 FE meshes and segmented images of femurs obtained from high-resolution peripheral quantitative computed tomography scans (HR-pQCT) [76] were obtained from Prof. Dieter Pahr, Head of the Biomechanics Research Group at TU Wien and a collaborator of this project's supervisor, Dr. Wolfram. The patient-specific information is not known and not directly relevant to this project. The dataset comprises of both left and right femurs, and for simplification in developing a framework to create the SSM, the left femurs (38/77) were extracted from the dataset and will be used.

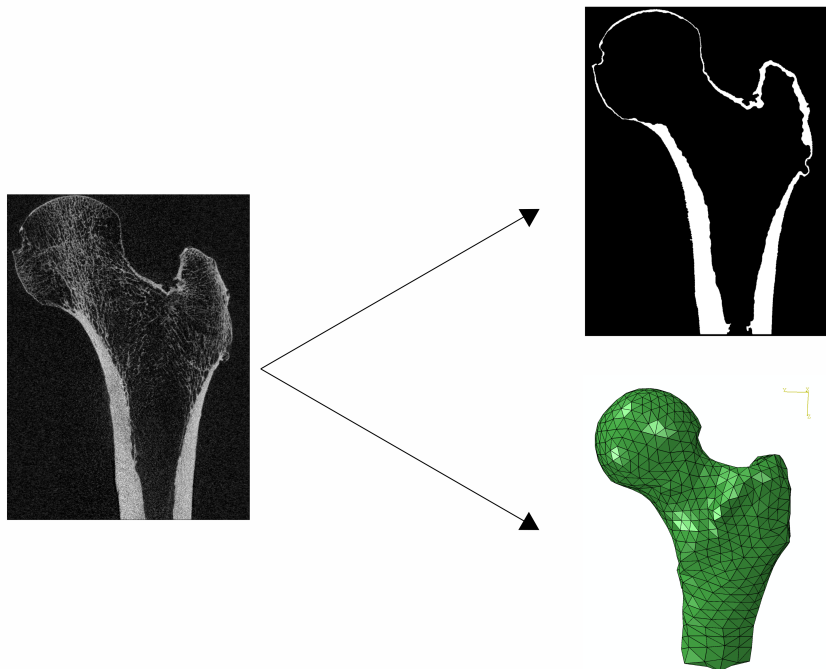


Figure 3: Illustration of dataset generated by Prof. Pahr. HR-pQCT image of a femur (left), gray value image segmenting the cortical shell (top right), and FE mesh (bottom right)

It was decided that Scalismo would be utilised to carry out this project, due to its versatility, stage of development, and availability of resources. Scalismo is implemented in Scala, and will be compiled in IntelliJ IDEA (JetBrains, Prague, Czechia)<sup>2</sup>. All code developed for use in this project is available in the supplementary folder.

---

<sup>2</sup><https://www.jetbrains.com/idea/>

## 4.2. Point Distribution Models

The PDM approach proposed by Cootes and Taylor approaches SSM generation by examining positional variation of anatomically significant, pre-defined *landmarks*. For example, consider a dataset of three polygons shown in Figure 4. Points 1 and 2 denote the leftmost corners of the polygon, and this convention is followed throughout all three shapes. All the other points are similarly labelled. Therefore, the mean position and positional variance for each point can be quantified, resulting in a mean overall shape and the main modes of variation of the entire shape quantified.

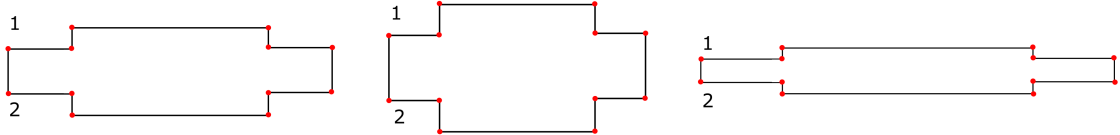


Figure 4: Example of a point-distribution model based on polygons resembling resistors, referencing Cootes and Taylor's original paper on PDMs [44]

Consider a dataset of  $n$  number of shapes from which a SSM will be built  $\{\Gamma_1, \dots, \Gamma_n\}$ . Each shape  $\Gamma_i$  can be described by a vector  $\mathbf{x}_i \in \mathbb{R}^{3N}$ , where the x, y, and z components of each point which make up the shape are represented until  $N$  number of points is reached.

$$\mathbf{x}_i = (x_{1x}^i, x_{1y}^i, x_{1z}^i, \dots, x_{Nx}^i, x_{Ny}^i, x_{Nz}^i) \quad (1)$$

From the vectorial description of the shapes, multivariate statistical analysis can be applied to analyse probabilistic variations of shape. It is assumed that a normal distribution is sufficient to describe shape variations [58].

$$\mathbf{x} \sim \mathcal{N}(\mu, \Sigma) \quad (2)$$

Where the mean shape  $\mu$  and the covariance matrix  $\Sigma$  can be calculated from the dataset.

$$\mu = \bar{\mathbf{x}} = \frac{1}{n} \sum_{i=1}^n \mathbf{x}_i \quad (3)$$

$$\Sigma = \frac{1}{n-1} \sum_{i=1}^n (\mathbf{x}_i - \bar{\mathbf{x}})(\mathbf{x}_i - \bar{\mathbf{x}})^T \quad (4)$$

Due to the large number of points being modelled in a 3D object, the covariance matrix would be too large to explicitly represent. Therefore, carrying out PCA [77] leads to the principal modes of variation in

the form of independent eigenvalues  $\lambda_i$  and associated eigenvectors  $\phi_i$ , where  $i = 1, \dots, n$ , being determined. This leads to the following description of the PDM.

$$\mathbf{x} = \bar{\mathbf{x}} + \sum_{i=1}^n \alpha_i \sqrt{\lambda_i} \phi_i \quad (5)$$

Where  $\alpha_i$  is a random coefficient and can be understood as a contrast which denotes the importance of each variation  $i$  identified by  $\lambda_i$  and  $\phi_i$

### 4.3. Modelling Approach

Two main approaches were identified for creating a shape model using the FE meshes; using the mesh itself or using the nodal data from the meshes, hereby referred to as the mesh approach and the node approach respectively. Previous studies described in the literature review have utilised a unified pipeline, wherein meshes are homologously generated from CT scans, resulting in meshes with the same number of nodes to avoid the registration problem. In the case of this study, each mesh has varying numbers of nodes and therefore registration will be an issue.

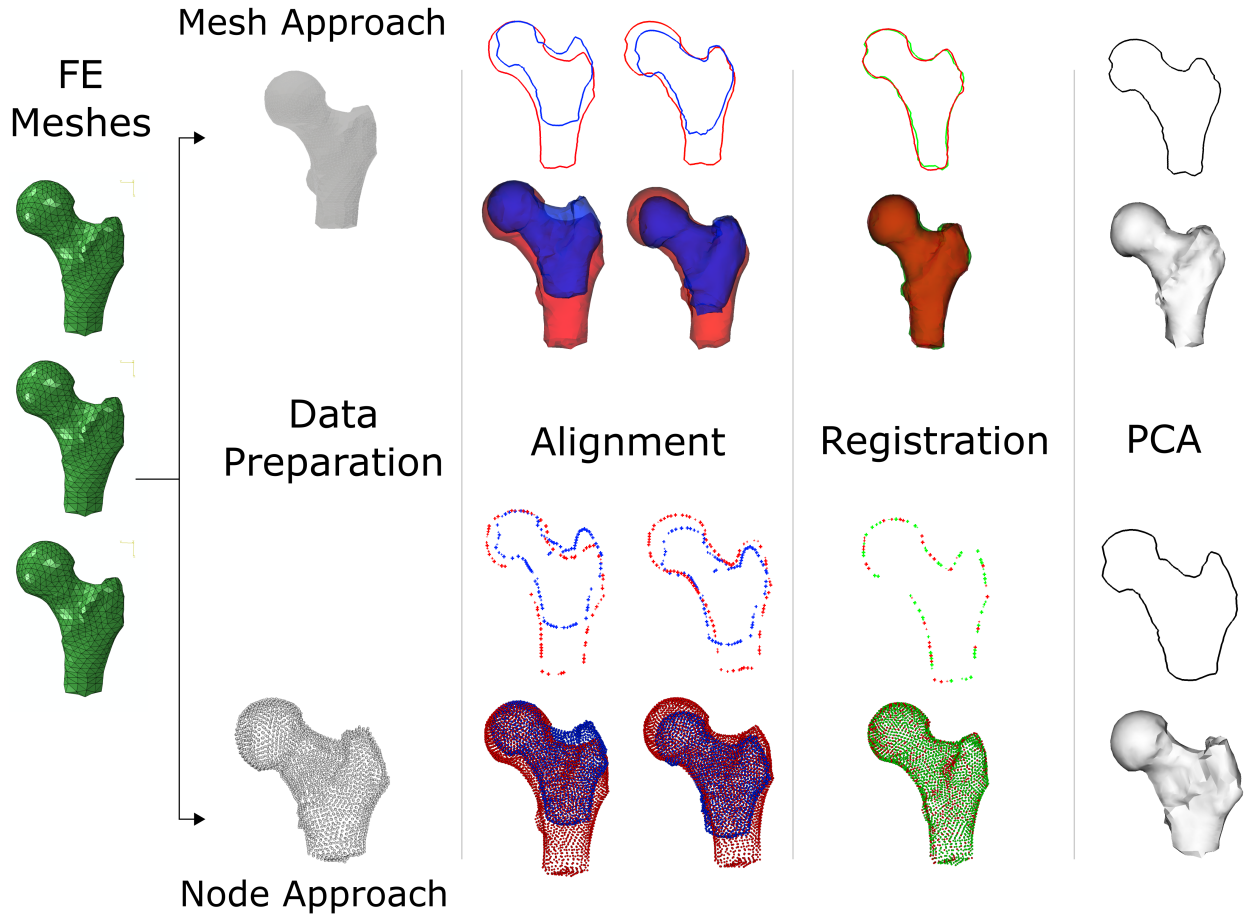


Figure 5: Overview of the two modelling approaches taken during this project. (From left to right) The input FE meshes are first prepared and converted to appropriate formats for input in a data preparation stage. Then, each femur is aligned to a common reference. Then, a reference femur is chosen and that femur is registered to the rest of the dataset. Finally, PCA is carried out to compute the shape model.

#### 4.4. Data Preparation

##### 4.4.1. Mesh Approach

The FE meshes were obtained as an Abaqus CAE (Dassault Systèmes, Vélizy-Villacoublay) input file (.inp) and therefore had to be converted to a format compatible with the Scalismo input-output functionality. The data meshes were first loaded into Abaqus, and exported as a Waveform 3D Object Files (.obj). The .obj files were then converted to stereolithography files (.stl) using Autodesk Inventor as Scalismo has a limited range of input file formats.

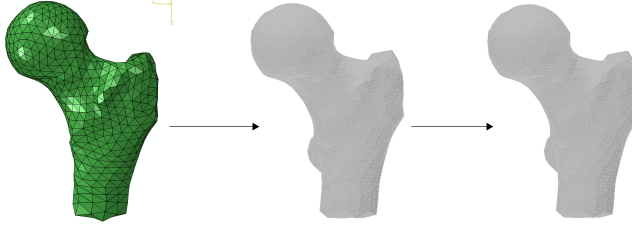


Figure 6: Pipeline utilised to convert .inp meshes to .stl. (From left to right) A .inp file is converted to a .obj file in Abaqus. Then the .obj file is loaded into Autodesk Inventor and converted to .stl format

#### 4.4.2. Node Approach

.inp files are arranged as headers followed by lists of nodes and elements. When Abaqus exports an .obj file from an .inp file, it takes the surface nodes from the mesh and forms them as a list of vertices and body polygons. From the .obj files, a Python script was coded to convert this into an indexed list of vertices, in essence a point cloud.

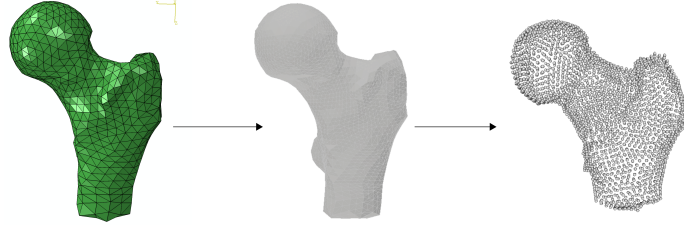


Figure 7: Pipeline utilised to convert .inp meshes to point clouds. (From left to right) A .inp file is converted to a .obj file in Abaqus. Then the .obj files are converted to a point cloud.

## 4.5. Alignment

The alignment of meshes can be described by Procrustes Analysis [78]. This is succinctly formulated as a minimization of the sum of distances  $D$  of each shape to the mean of the dataset (Equation 6) [61].

$$D = \min \sum_{i=1}^n |\mathbf{x}_i - \bar{\mathbf{x}}|^2 \quad (6)$$

In both the mesh and node approach, an ICP rigid alignment algorithm was utilised as outlined in Algorithm 1 [59, 60].

---

**Algorithm 1:** Iterative closest points algorithm for rigid alignment

---

**Input:**  $\Gamma_R$ ,  $\Gamma_T$ , Number of Iterations  
**Output:**  $\Gamma_{T,aligned}$

**begin**

**repeat**

**foreach**  $x_i \in \Gamma_T$  **do**

Find closest point on  $\Gamma_R$

Attribute as correspondences

Transform  $\Gamma_T$  to minimize distance with  $\Gamma_R$

Number of Iterations - 1

**until** Number of Iterations = 0

---

The main difference in the alignment step for the mesh and node approach is the input file format, with the former being a mesh and the latter being a point cloud. Therefore the ICP algorithm was modified accordingly to account for the different input syntax. Although the ICP algorithm has been criticised for being prone to being stuck in local minima [53], due to the relatively geometrically simple shape of femurs in comparison to other complex anatomical structures, the ICP algorithm could still be robust in its use [79].

## 4.6. Correspondence and PCA

For a dataset of shapes  $\{\Gamma_1, \dots, \Gamma_n\}$ , if each shape is derived from an arbitrary reference shape  $\Gamma_R$ , it can be said that every point on each shape within the dataset has a *corresponding* point which is also present on every other shape in the dataset. This allows for statistical analysis of the variation of each point across the dataset, alongside possible covariance of each point i.e. the construction of the shape model [44].

However, in reality correspondence is not always automatically established due to inherent variations present across a varied dataset i.e anatomical, size, etc. The establishment of correspondence, also known as the *registration problem* is an active field of research. The use of consistent and anatomically significant landmarks manually placed across a dataset is the 'golden standard', however for a 3D shape, the process of manual landmarking is tedious and prone to operator error. A comparison of the registration of two hands is shown in Figure 8.

### 4.6.1. Mesh Approach

In the mesh approach, a parametric non-rigid registration proposed by Lüthi et al was followed [58, 80]. With an arbitrarily chosen reference shape  $\Gamma_R$ , a Gaussian process can be defined with a zero mean and a synthetic kernel. Registration can also be formulated as an optimization problem on the basis of Bayesian statistics shown in Equation 7 [58].

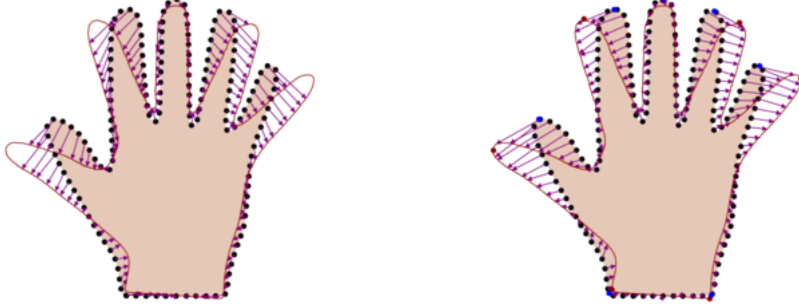


Figure 8: Comparison of correspondence in two examples [80]. (Right) Every point on the reference (solid shape with dotted outline) has a corresponding point on a target shape (purple outline) and this is matched correctly. (Left) The correspondence is not accurately attributed i.e. the point on the tip of the thumb is not matched correctly onto the target shape.

$$\arg \min_u \mathcal{D}[\Gamma_R, \Gamma_T, u] - \eta \ln p(u) \quad (7)$$

Where  $u$  is a deformation which exists that transforms  $\Gamma_R$  to  $\Gamma_T$ ,  $\mathcal{D}$  is a metric that measures the similarity of both shapes,  $p(u)$  is a Gaussian process prior over the admissible deformation fields, and  $\eta \in \mathbb{R}$  is a weighting parameter.

When Equation 7 is reinstated in a parametric form and combined with a low-rank approximation of the Karhunen-Loëve expansion of the Gaussian process shown in Equation 8, this leads to an efficient formulation to create an algorithm for registration shown in Equation 9. Therefore, Equation 9 can then be minimized in a quasi-ICP algorithm to fit the reference mesh to the rest of the dataset, establishing correspondence [58].

$$\tilde{u}(x) \sim \mu(x) + \sum_{i=1}^r \alpha_i \sqrt{\lambda_i} \phi_i(x) \quad (8)$$

$$\arg \min_{\alpha_1, \dots, \alpha_r} \mathcal{D} \left[ \Gamma_R, \Gamma_T, \mu + \sum_{i=1}^r \alpha_i \sqrt{\lambda_i} \phi_i \right] + \eta' \sum_{i=1}^r \alpha_i^2 \quad (9)$$

The flexibility of the shape model constructed from the synthetically defined Gaussian process can be enhanced by using a combination of kernels, the so called multi-scale approach [70]. In this paper, a multi-scale approach in defining kernels was followed as it has been shown to be more effective than utilising standard kernels [58]. Three synthetic kernels were defined with  $\sigma$  and  $s$  values of 90 and 150, 40 and 5, and 10 and 3. These values were arbitrarily determined based on rule of thumb anecdotes from the Scalismo

community to model femurs.

1000 points were randomly sampled from a mesh with the median number of nodes of the dataset. These were then utilised to define a synthetic shape model. From this shape model, 5000 points uniformly distributed across the shape model were then utilised in an iterative fitting process to fit to each target shape in the dataset. The difference in sampled points to generate the interim SSM and initiate registration is due to computational limits. The higher the number of points utilised to define a SSM, the more taxing the computational load. Figure 9 demonstrates the effectiveness of the iterative nature of the registration process, with each iteration, the fitting of the reference-defined interim SSM onto the target shape improves incrementally.

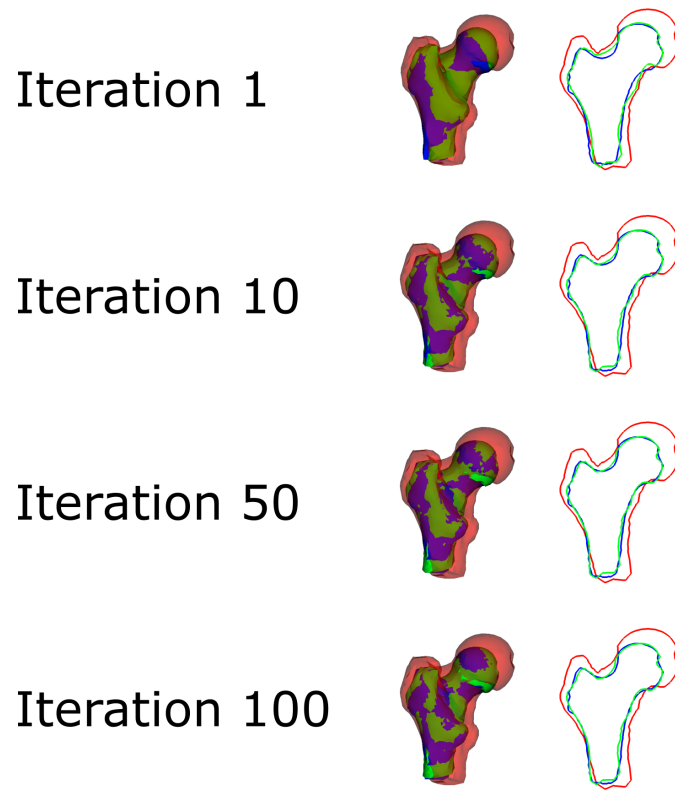


Figure 9: Illustration of iterative registration process. The red mesh is the reference mesh, blue is target mesh, and green is the resulting fit after the corresponding number of iterations.

#### 4.6.2. Node Approach

In the node approach, an adaptation of the ICP algorithm is proposed. Similar to the mesh approach, the smallest point cloud was chosen and defined as a Gaussian process with a zero mean and synthetic kernel. This interim SSM is then fitted to target meshes in an iterative process. After a set number of iterations, the fitted point cloud will be very close in shape to the target clouds. A final correspondence step takes place, wherein the closest points between the post-recursion model and the target shape are attributed as corresponding points.

This final closest points correspondence attribution step is formed on the basis that if every single node of the reference point cloud is anatomically significant and has a corresponding point on every other femur in the dataset, this would effectively ensure a more accurate correspondence step by eliminating the average and Hausdorff distances post-registration.

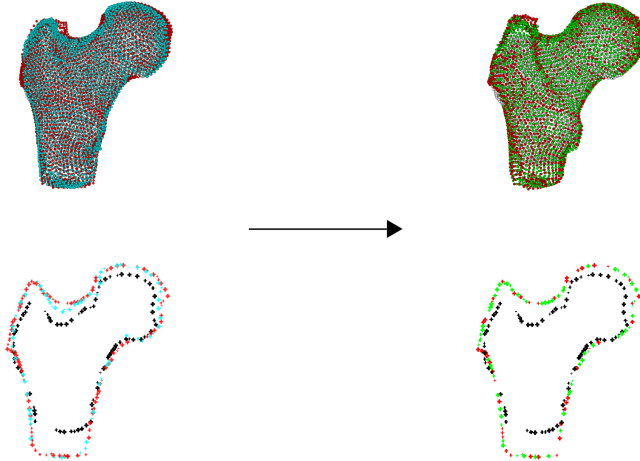


Figure 10: Illustration of nodal alignment. Red point cloud is target, white/black is reference, cyan is post-recursive registration, and green is final attributed closest points. After a recursive fitting procedure (left), the closest points of the resulting point cloud to the target mesh are attributed as correspondences (right)

#### 4.6.3. Principal Component Analysis

The PCA step is integrated within Scalismo functionality. A function in the Scalismo library can be called and allows for the creation of a shape model easily. In the mesh approach this step is relatively straightforward, utilising a data collection function which is able to collect every mesh from a folder and generate a shape model from that. In the node approach, as each deformation field calculated by the PCA is associated with each node of the point cloud, these deformation fields are then reassigned with the reference mesh which results in a shape model incorporating the variation of every point of the reference mesh.

The results of the PCA are utilised in defining  $\lambda_i$  and  $\phi_i$ . With each  $\lambda_i$  and its associated  $\phi_i$  values being denoted as an *eigenmode*. Where the earlier eigenmodes denote the principal variations i.e. the variations most present in the dataset.

After the PCA step, the resulting mean mesh in the mesh approach was utilised to rerun the alignment, registration, and PCA steps. By utilising the mean of the dataset to initiate alignment and registration, unwanted statistical biases towards the selected reference mesh is minimised. In contrast, the node approach registration relies on the final association step to produce good correspondences. Note that all code used throughout this project is available in the supplementary folder.

## 5. Results and Discussion

The results of alignment, registration, and the final PCA will be discussed in this section. As mentioned previously, after an initial alignment, registration, and PCA, the mean shape was utilised as the new reference mesh in a second iteration of the pipeline. For simplification, the initial pipeline alignment and registration steps will be discussed and evaluated, whilst the secondary step will not. Likewise, only the final PCA models will be discussed whilst the interim models will not.

### 5.1. Alignment Evaluation

The alignment step was evaluated by measuring the average distances and the Hausdorff distances between the target and reference shape pre and post alignment. The average distances are obtained by calculating the distance between each vertex of the target and reference shape. The Hausdorff distance is the maximum distance between the target and reference object [81] and is similarly obtained. Both measures are integrated in Scalismo as functions and those were simply used in the mesh approach. For the node approach however, Scalismo does not support evaluation of point clouds and these functions had to be independently coded in Scala. Femurs 604 and 587 were chosen as reference femurs for the node and mesh approach respectively. The former due to it being the smallest mesh and would ease the registration step and the latter being the median mesh and similarly the registration step would be eased. The average and Hausdorff distances for each femur in both approaches, denoted by their Femur ID as specified in the dataset, are graphically illustrated in Figures 12 - 15.

In the node approach, almost every mesh shows good compliance with the alignment algorithm, showing a decrease in the average and Hausdorff distances in Figures 12 and 13 respectively. On average, there is a 26.3% decrease in average distance and a 29.7% decrease in the Hausdorff distance of the entire dataset. In the mesh approach, every mesh shows compliance with the alignment algorithm as shown in Figures 14 and 15, with a 40.3% decrease in average distance and a 36.12% decrease in Hausdorff distance across the entire dataset on average.

In Figure 12 outliers such as Femur 611, 641, and 671 show an increase in average distance rather than a decrease. This is due to the significant size difference between said meshes and the reference mesh. The alignment algorithm resulted in the target and reference femurs' centre of masses aligning resulting in the distance of each node of the reference and target effectively increasing due to the remarked size difference. This is visualised in Figure 11. When the Hausdorff distances of the aforementioned meshes are compared, they show a decrease rather than an increase in line with the average distances, denoting that in fact alignment has occurred. A similar argument is posed for the Hausdorff distance outliers in Figure 13. These outliers exemplify the need for the use of multiple metrics to evaluate mesh alignment as one metric may not effectively describe the results of the alignment process.

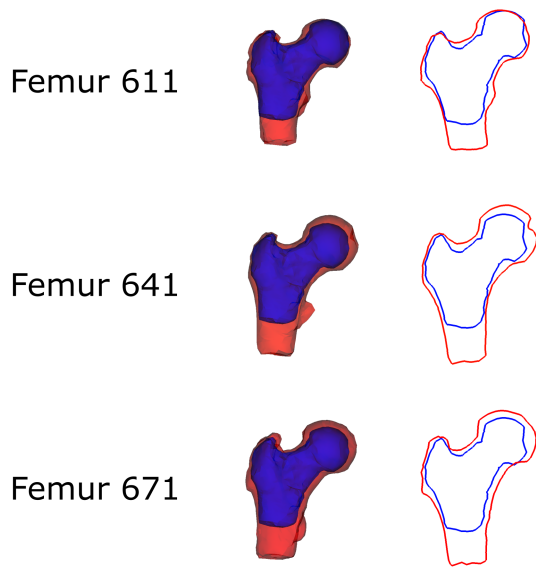


Figure 11: Source of alignment discrepancies visualised. In all three outliers, the length of the femur from the lower trochanter leading to the rest of the femur is seen to be much longer in the target (red) than the reference (blue) leading to increased average distances

Overall it can be noted that the average and Hausdorff distances in the node approach are significantly higher than in the mesh approach. This is due to the functions utilised to evaluate these metrics. The node approach required specific functions to be created as the Scalismo library did not support point cloud evaluation. These functions rely on a "findClosestPoint" function which takes a reference point on a point cloud and finds the closest point on a target point cloud. In contrast, the mesh approach function inbuilt into Scalismo utilises a "closestPointOnSurface" function which finds the distance between a reference point on a reference mesh and the surface of a target mesh. In determining the closest points between two point clouds, the relative locations of both point clouds in Euclidean space could result in the closest points being determined by a vectorial description requiring the use of relative angles, whilst in determining the closest points between a point and a surface, a simple normal vector can be used resulting in relatively lower distances. Nevertheless, both metrics in both approaches show a general decrease which denotes that

alignment of point clouds and meshes has taken place. The key deficiency in the approach taken in this study is the arbitrarily assigned number of iterations. A possible evaluation step could be inbuilt into the ICP algorithms utilised, wherein instead of inputting a number of iterations, a recurring function could be formulated which continuously evaluates the percentage decrease in average and/or Hausdorff distances between two meshes and if a point is reached where an increasing number of iterations does not significantly decrease the desired metric, a convergence of sorts is reached and the ideal number of iterations is found.

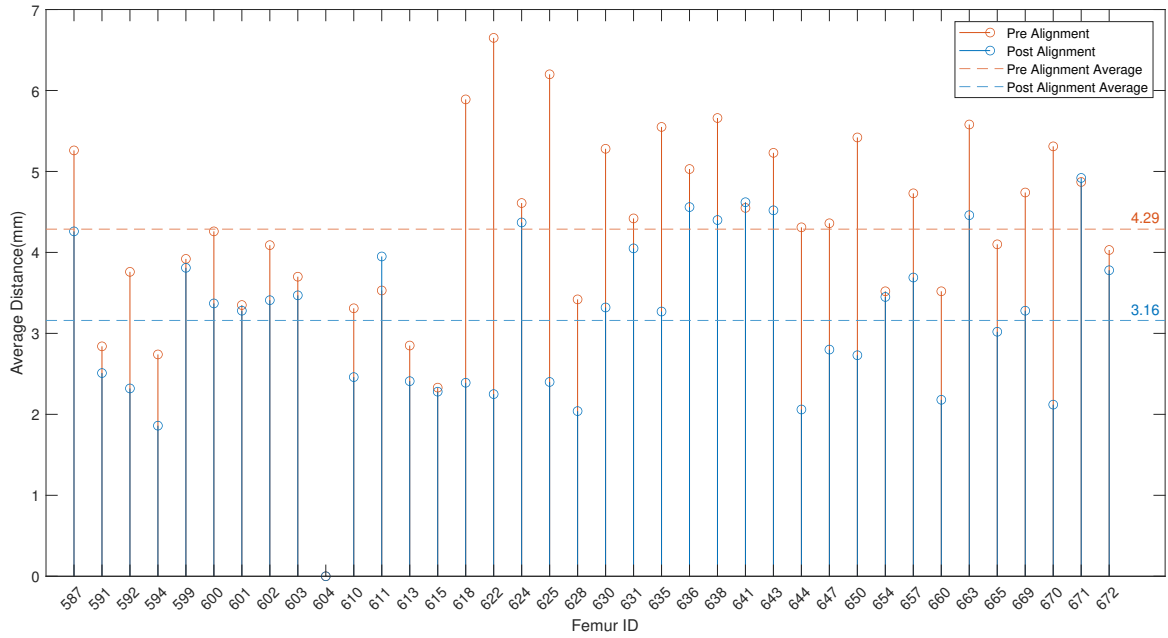


Figure 12: Alignment evaluation of node approach based on average distances pre and post alignment

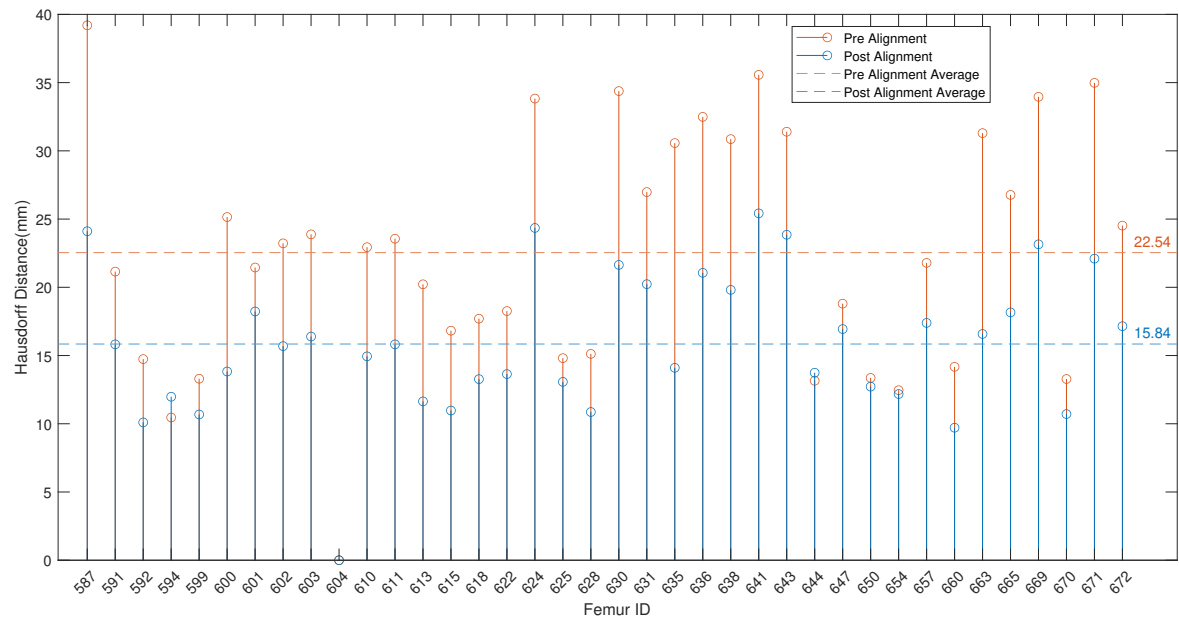


Figure 13: Alignment evaluation of node approach based on Hausdorff distances pre and post alignment

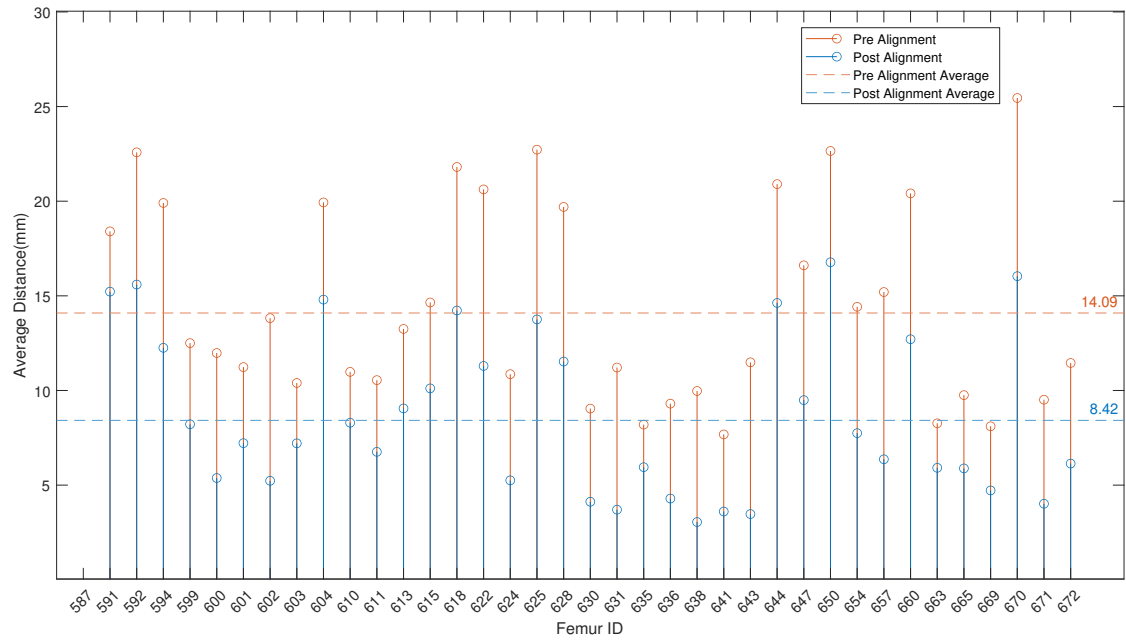


Figure 14: Alignment evaluation of mesh approach based on average distances pre and post alignment

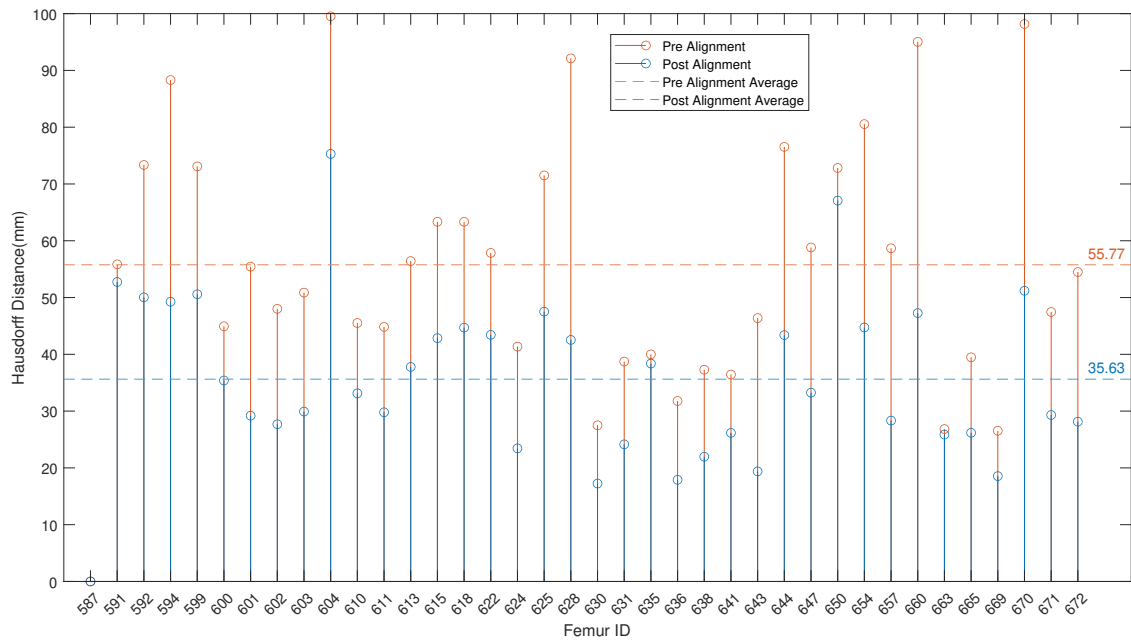


Figure 15: Alignment evaluation of mesh approach based on Hausdorff distances pre and post alignment

## 5.2. Registration Evaluation

Similarly to alignment, the registration metrics are average and Hausdorff distances. Figures 17 and 18 show results from the registration of the meshes in the node and mesh approaches respectively. In the node approach, similarly to the alignment step, Femur 604 was chosen as the reference femur as it was the smallest point cloud whilst in the mesh approach Femur 624 was chosen as it was the median mesh.

In the node approach the average of the average distances is 1.65mm and the average Hausdorff distance is 7.45mm. Whilst in the mesh approach, the average of the average distances is 1.84mm whilst the average Hausdorff distance is 13.54mm. A key difference in the results could again be due to the difference in functions utilised to quantify the selected metrics. The registration algorithm proposed for the node approach could function better due to each node being registered in contrast with the mesh approach where a discrete set of uniformly distributed points, much lower in number than the actual number of vertices, are used instead. This could highlight the importance of utilising as larger numbers of landmarks in initializing registration. Similarly to the alignment algorithm, the number of uniformly distributed points sampled for the mesh alignment was arbitrarily set at 5000, and the number of iterations was arbitrarily set at 100 as well. To increase the algorithm's effectiveness and save on computational load, an optimisation function could be incorporated which continually evaluates the desired metrics to determine optimal number of points and iterations.

When comparing the mesh approach registration to similar works such as the work by Fouefack, he reported average Hausdorff distances of 0.7 mm and 1.28 mm in registration of humeri and scapulae respectively [82]. Lüthi et al. reported average distances of 0.6 - 0.65 mm and Hausdorff distances of 3 - 4 mm when utilising a similar multiscale registration approach for ulnas [58]. The stark difference in registration results could be due to the nature of the meshes in the dataset utilised in this study. The femur meshes were generated from FE meshes, which are inherently 'jagged' due to the nature of the tetrahedral elements which make up a FE mesh. In converting the FE meshes to stl formats the 'jaggedness' of the meshes are inherited throughout the conversion pipeline as demonstrated in Figure 16. In contrast, the meshes utilised by Fouefack and Lüthi et al. are much smoother as they did not originate from FE meshes. The smoothness of the meshes allowed for much more stable performance of the registration algorithms in fitting the reference meshes to target meshes. A potential solution to remedy the unsatisfactory registration could be in restructuring the entire modelling pipeline. Rather than generating FE meshes directly from CT imaging, smoother more accurate meshes could be generated instead and used in shape modelling. From a shape model built from smooth meshes, FE meshes can then be generated and used for patient-specific FEA. If FE meshes are essential to the pipeline, potentially increasing the number of elements to smoothen the mesh would improve registration results. Otherwise, the registration approach should be reevaluated and alternative avenues should be explored.

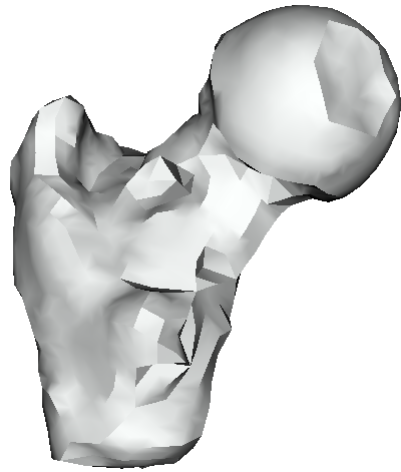


Figure 16: Post alignment mesh during the mesh approach. The 'jagged' nature of the surfaces along the femoral neck and the greater trochanter are noted due to the initial mesh being a finite element mesh

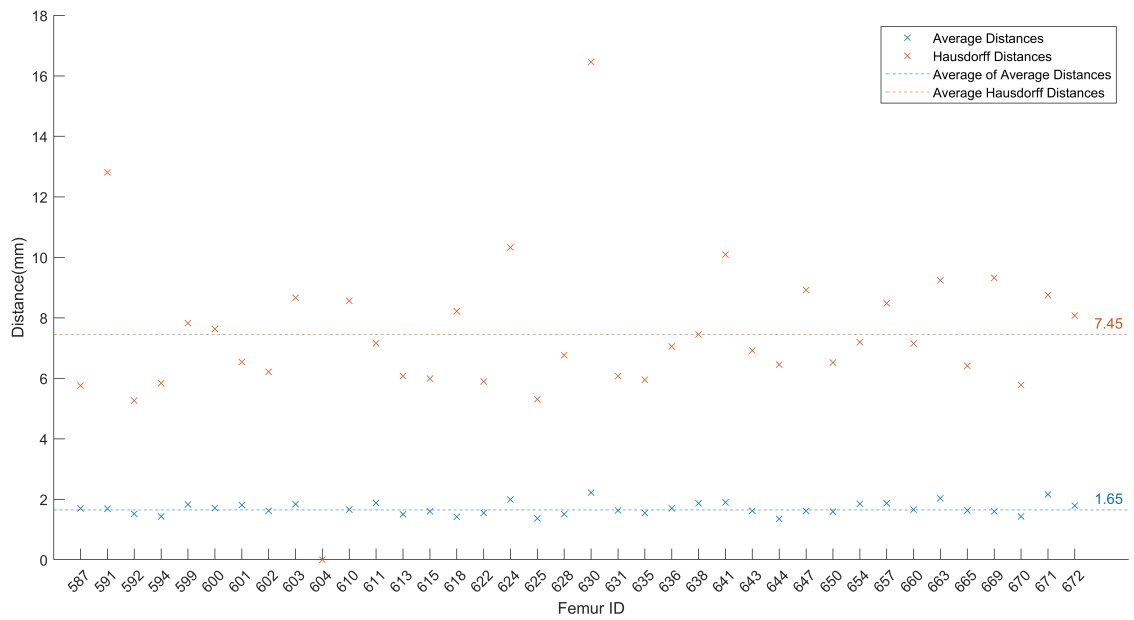


Figure 17: Registration evaluation of node approach based on average and Hausdorff distances

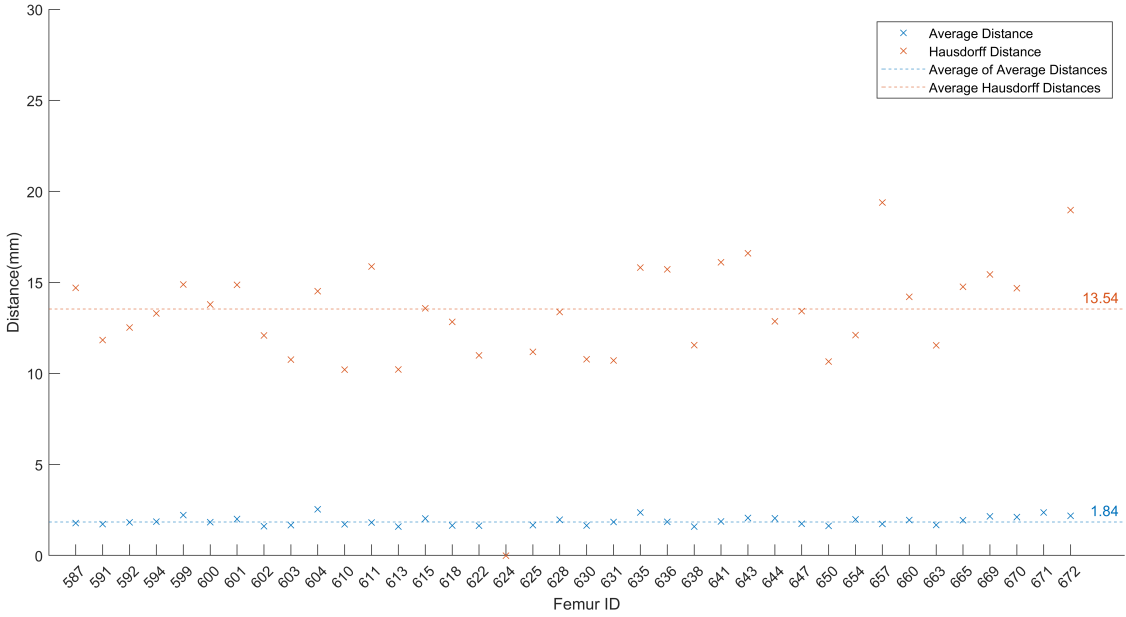


Figure 18: Registration evaluation of mesh approach based on average and Hausdorff distances

### 5.3. Model Evaluation

The mean meshes of the SSMs resulting from the node and mesh approach can be seen in the middle column of Figure 19. Figure 20 illustrates the percentage of variation captured in each eigenmode for the node and mesh approaches. It also illustrates the cumulative variance captured with each eigenmode. It can be noted that in the mesh approach the initial eigenmodes are able to capture a much higher percentage of variation in comparison with the node approach. This is reflected overall with the cumulative variance curve of the mesh approach being much steeper and therefore capturing a larger amount of variation in fewer eigenmodes. This denotes that the mesh approach shape model is much more *compact* than the node approach shape model. *Compactness* can be defined as the cumulative described variance of each eigenmode, where a higher compactness means that less variables are needed for a shape model to describe population variance [83].

From Figure 19 the variation each eigenmode represents is shown.<sup>3</sup> In terms of the mesh approach, Mode 1 is shown to represent the overall size of the femur. Mode 2 represents the length below the lesser trochanter leading to the rest of the femur. This mode in particular is not anatomically significant as this length originates from the segmentation process. This could highlight an important facet of segmentation to generate meshes for use in SSMs, in that the segmentation line on the femur should be uniformly placed when generating meshes. Mode 3 and 4 are similar in that they represent the length of the femoral neck and the size of the greater and lesser trochanters. The former seemingly incorporates a tilt of the overall femur and focuses on the length lower femoral neck. Whilst the latter incorporates little tilt and instead focuses on

<sup>3</sup>A diagram briefly describing anatomically significant areas of interest of a femoral head is located in the Appendix.

the upper part of the femoral neck. Mode 4 also seemingly describes the variation of the angle between the greater and lesser trochanters. The fact that similar variations are represented by two separate eigenmodes could highlight a deficiency in the computing of the shape model, wherein the shape model could be more compact by combining these eigenmodes. If alternate shape model computing methods are utilised and this discrepancy is still present, it could be of note that the extension of the upper and lower parts of the femoral neck are discrete variations. Mode 5 represents the height/size of the upper trochanter.

In terms of the node approach however, the variations are not as clear. Mode 1 seemingly represents the overall size. Mode 2 seems to represent the length of the femoral neck. Mode 3 represents the size of the upper and lower trochanters. Mode 4 seems to represent the femoral neck length as well, and Mode 5 seemingly does not have represent clear variation. Furthermore, as shown in Figure 20 the presence of more eigenmodes in the node approach means that the variations are much more spread out and the SSM overall is less compact. The clear discrepancy in visible variation captured could be due to inaccurate registration. In assuming that every point in the smallest mesh had a corresponding point on every other mesh, the registration algorithm was in turn biased towards the shape of the reference mesh. This is reflected in the unsatisfactory SSM generated producing unclear variations, possibly resulting from unsatisfactory covariations being defined. In contrast, by sampling a uniformly distributed number of points throughout each dataset as in the mesh approach, the distribution of quasi-landmarks in turn are shown to result in better registrations.

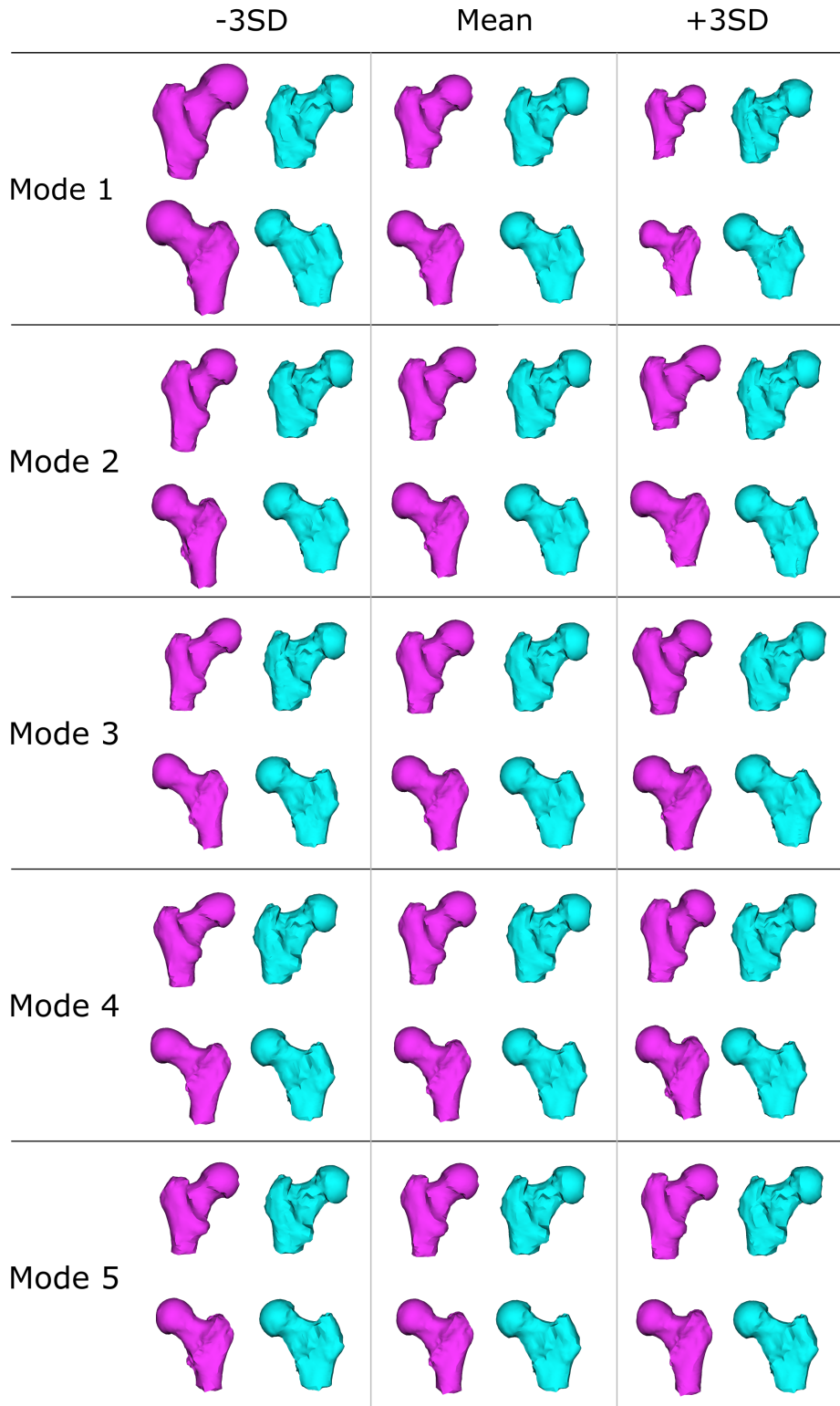


Figure 19: Comparison of the shape models generated by the node approach (cyan) and mesh approach (magenta) in terms of the deformations represented by the first five eigenmodes. For each eigenmode, the mean, -3 standard deviations, and +3 standard deviations are shown for two sides of the meshes.

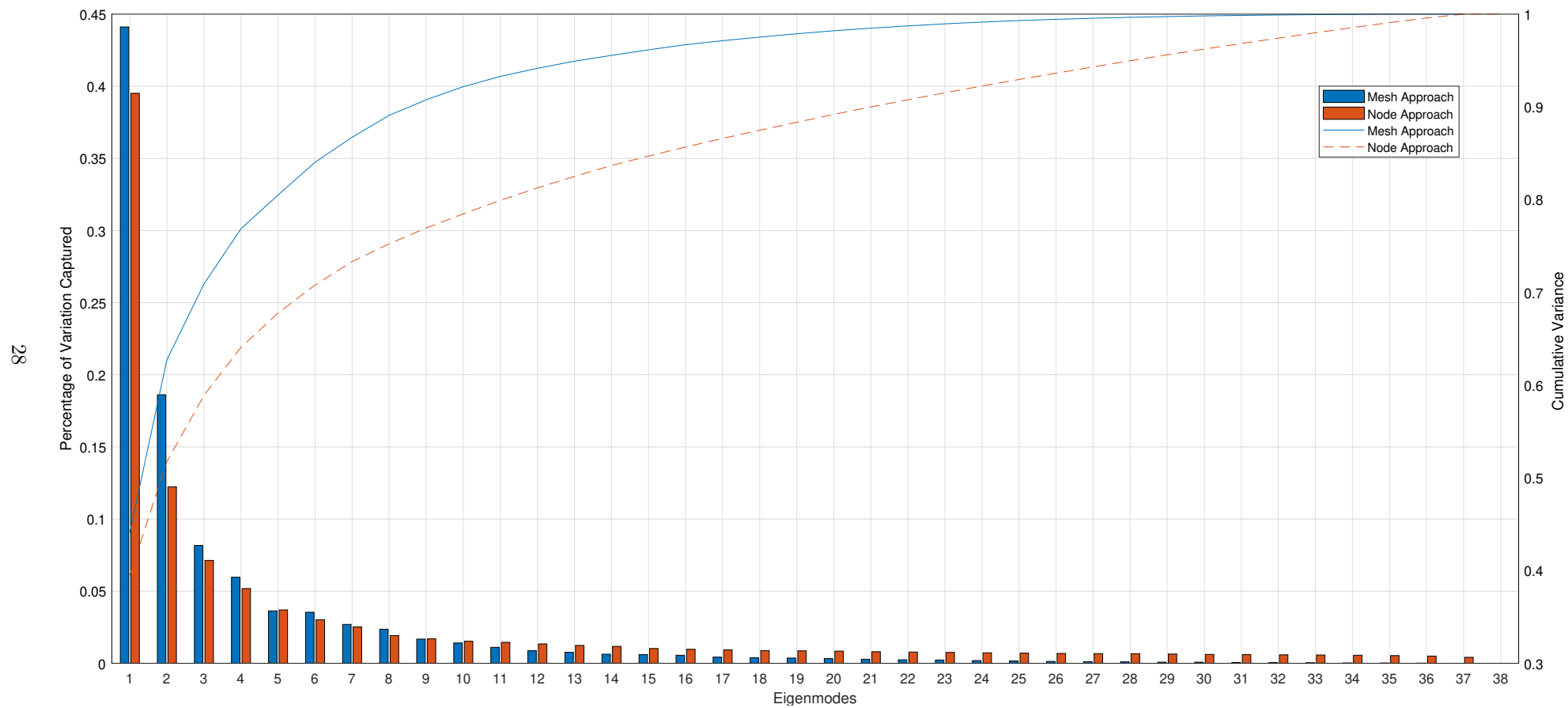


Figure 20: Cumulative variance captured by each respective eigenmodes of the node and mesh approach.

## 6. Conclusions and Further Work

In this project, two approaches to generating SSMs of femurs were investigated. ICP algorithms for dataset alignment were utilised followed by non-rigid registration algorithms. Both steps were evaluated by means of average and Hausdorff distances. It was found that overall the alignment step for both approaches was effective, and possible improvements were outlined. In terms of the registration step, results were not satisfactory when compared with existing works. Key sources of error were highlighted and possible methods to improve this step were outlined as well. The generated shape models were compared and it was found that the mesh approach was superior to the node approach, as the generated shape model was found to be much more compact and the variations described by each eigenmode are clearer.

The registration step is the key source of error in the pipeline presented in this work and needs to be improved in future iterations, either by re-examining the initial mesh generation or expanding the search for an optimal registration technique for FE meshes. Overall it was quantitatively proven that the mesh approach is the better of the two proposed approaches and in future works incorporating statistical shape modelling of femurs from a dataset utilising FE meshes, the mesh approach is recommended over the node approach.

A generated SSM can be utilised to create a SSAM. Similar to works by Humbert et al. [56], Nolte and Bull [71], and Chandran et al. [69], SSAMs of femurs have the potential to be able utilised to be used instantly generate FE meshes of femurs from DXA imaging through means of the active appearance model framework [84]. The ability to easily generate patient-specific FE models for use in personalised fracture risk assessments is a major step forward in the road towards personalised healthcare for the better in modern society. The creation of a SSM in this paper is a major step forward towards this goal and the techniques and methodologies presented in this work will positively contribute towards future works looking to further this field of research.

## 7. Acknowledgements

I would like to thank the Graphics and Vision Research Group in the University of Basel for developing Scalismo as open access and thus making the field of statistical shape modelling field more accessible. Furthermore, I'd like to thank the Scalismo community in supporting me and answering some of my questions as to how to utilise Scalismo effectively.

I would also like to thank Prof. Pahr, Head of Computational Biomechanics at TU Wien for providing us with a copy of the dataset used in this project.

I'd also like to thank my supervisor Dr. Wolfram for encouraging me and supporting me in pursuing such a challenging and complex topic in an active field of research usually reserved for masters or doctorate level students in the field of computer science or mathematics.

I'd also like to thank my friends and family for supporting me throughout my undergraduate studies.

一个篱笆三个桩，一个好汉三个帮

## References

- [1] United Nations Department of Economic and Social Affairs, "World population ageing," 2017.
- [2] E. Jaul and J. Barron, "Age-related diseases and clinical and public health implications for the 85 years old and over population," *Frontiers in Public Health*, vol. 5, no. 335, 2017.
- [3] A. El Maghraoui and C. Roux, "Dxa scanning in clinical practice," *Q J Med*, vol. 101, pp. 605–617, 2008.
- [4] A. Unnanuntana, B. Gladnick, *et al.*, "The assessment of fracture risk," *The Journal of Bone and Joint Surgery, Incorporated*, no. 92, pp. 743–53, 2010.
- [5] J. Pasco, E. Seeman, *et al.*, "The population burden of fractures originates in women with osteopenia, not osteoporosis," *Osteoporosis International*, no. 17, pp. 1404–1409, 2006.
- [6] D. Cody, G. Gross, *et al.*, "Femoral strength is better predicted by finite element models than qct and dxa," *Journal of Biomechanics*, no. 32, pp. 1013–1020, 1999.
- [7] S. Young, M. Safran, and M. Clatworthy, "Applications of computer navigation in sports medicine knee surgery: an evidence based review," *Current Reviews in Musculoskeletal Medicine*, no. 6, pp. 150–157, 2013.
- [8] M. V., T. M., *et al.*, "Reverse engineering of human bones by using method of anatomical features," *CIRP Annals - Manufacturing Technology*, no. 62, pp. 167–170, 2013.
- [9] S. Väänänen, J. Jurvelin, and H. Isaksson, "Estimation of 3d shape, internal density and mechanics of proximal femur by combining bone mineral density images with shape and density template," *Biomechanics and Modeling in Mechanobiology*, no. 11, pp. 791–800, 2012.
- [10] D. Runde, B. Godbout, *et al.*, "Radiation exposure among highest ct scan utilizers," *Annals of Emergency Medicine*, no. 86, 2011.
- [11] D. Schwartz, "Counter-Point: Are We Really Ordering Too Many CT Scans?," *The Western Journal of Emergency Medicine*, vol. 4, no. 2, pp. 120–122, 2008.
- [12] M. Brainin, Y. Teuschl, and L. Kalra, "Acute treatment and long-term management of stroke in developing countries," *Lancet Neurol*, no. 6, pp. 553–61, 2007.
- [13] T. Cootes and C. Taylor, "Anatomical statistical models and their role in feature extraction," *The British Journal of Radiology*, no. 77, pp. 133–139, 2004.
- [14] T. Heimann and H. Meinzer, "Statistical shape models for 3d medical image segmentation: A review," *Medical Image Analysis*, no. 13, pp. 543–563, 2009.
- [15] F. Cosman *et al.*, "Clinician's guide to prevention and treatment of osteoporosis," *Osteoporosis International*, no. 25, pp. 2359–2381, 2014.
- [16] T. Sözen *et al.*, "An overview and management of osteoporosis," *European Journal of Rheumatology*, no. 4, pp. 46–56, 2016.
- [17] P. Shan, C. Xian, *et al.*, "Osteoporosis," *International Journal of Endocrinology*, 2013.
- [18] M. Nanes and C. Kallen, "Osteoporosis," *Seminars in Nuclear Medicine*, no. 44, pp. 439–450, 2014.
- [19] C. Cooper, G. Campion, and L. Melton, "Hip fractures in the elderly: A world-wide projection," *Osteoporosis International*, vol. 2, pp. 285–289, 1992.
- [20] International Osteoporosis Foundation, "Broken Bones, Broken Lives: A road map to solve the fragility fracture crisis in the United Kingdom," tech. rep., International Osteoporosis Foundation, 2018.
- [21] D. Dempster, E. Shane, *et al.*, "A simple method for correlative light and scanning electron microscopy of human iliac crest bone biopsies: qualitative observations in normal and osteoporotic subjects," *Journal of Bone and Mineral Research : The Official Journal of The American Society for Bone and Mineral Research*, vol. 1, pp. 15–21, February 1986.
- [22] P. Conaghan *et al.*, *Osteoarthritis: National clinical guideline for care and management in adults*, ch. 1. Royal College of Physicians, 2008.
- [23] S. Glyn-Jones, A. Palmer, *et al.*, "Osteoarthritis," *Lancet*, vol. 386, pp. 376–387, 2015.
- [24] N. Arden and M. Nevitt, "Osteoarthritis: Epidemiology," *Best Practice and Research Clinical Rheumatology*, vol. 20, no. 1, pp. 3–25, 2006.
- [25] A. Woolf and B. Pfleger, "Burden of major musculoskeletal conditions," *Bulletin of The World Health Organization*, vol. 81, pp. 646–656, 2003.

- [26] S. Odella, A. Querenghi, *et al.*, “Trapeziometacarpal osteoarthritis: pyrocarbon interposition implants,” *Joints*, vol. 2, no. 4, pp. 154–158, 2014.
- [27] G. Pisanu, F. Rosso, B. C., *et al.*, “Patellofemoral arthroplasty: Current concepts and review of literature,” *Joints*, vol. 5, no. 4, pp. 237–245, 2017.
- [28] A. Hughes, C. DeBuitleir, P. Soden, *et al.*, “3d printing aids acetabular reconstruction in complex revision hip arthroplasty,” *Advances in Orthopaedics*, 2017.
- [29] American Academy of Orthopaedic Surgeons, “Arthritis of the knee.” <https://orthoinfo.aaos.org/en/diseases-conditions/arthritis-of-the-knee/>, June 2014.
- [30] J. Cooper, J. Lewis, and J. Lord, “Healthcare expenditure, UK Health Accounts: 2017,” 2017.
- [31] Eurostat, “Healthcare expenditure statistics,” 2019.
- [32] National Institute for Health and Care Excellence, “Glossary.” <https://www.nice.org.uk/Glossary?letter=Q>.
- [33] B. Orenstein, “How Osteoporosis Can Affect Your Emotional Health.” <https://www.everydayhealth.com/hs/osteoporosis-bone-health/emotional-effects-osteoporosis/>, 2015.
- [34] M. Kass, A. Witkin, and D. Terzopoulos, “Snakes: Active Contour Models,” *International Journal of Computer Vision*, vol. 1, pp. 321–331, 1988.
- [35] D. Terzopoulos, A. Witkin, and M. Kass, “Constraints on Deformable Models: Recovering 3D Shape and Nonrigid Motion,” *Artificial Intelligence*, vol. 36, pp. 91–123, 1988.
- [36] J. Montagnat, H. Delingette, and N. Ayache, “A review of deformable surfaces: topology, geometry and deformation,” *Image Vision Computing*, vol. 9, no. 14, pp. 1023–1040, 2001.
- [37] S. Osher and J. Sethian, “Fronts Propagating with Curvature-Dependent Speed: Algorithms Based on Hamilton-Jacobi Formulations,” *Journal of Computational Physics*, vol. 79, pp. 12–49, 1988.
- [38] R. Malladi, J. Sethian, and B. Vemuri, “Shape Modeling with Front Propagation: A Level Set Approach,” *IEEE Transactions On Pattern Analysis And Machine Intelligence*, vol. 17, no. 2, pp. 158–175, 1995.
- [39] A. Saito, M. Tsujikawa, T. Takakuwa, *et al.*, “Statistical Shape Model of Nested Structures Based on the Level Set,” in *Medical Image Computing and Computer Assisted Intervention - MICCAI 2017*, pp. 169–176, Springer International Publishing, 2017.
- [40] C. Woods, C. Fernee, M. Browne, *et al.*, “The potential of statistical shape modelling for geometric morphometric analysis of human teeth in archaeological research,” *PLOS ONE*, vol. 12, no. 12, 2017.
- [41] M. Fuessinger, S. Schwarz, C. Cornelius, *et al.*, “Planning of skull reconstruction based on a statistical shape model combined with geometric morphometrics,” *International Journal of Computer Assisted Radiology and Surgery*, vol. 13, no. 4, pp. 519–529, 2018.
- [42] S. van Dongen, F. Danckaers, *et al.*, “Women’s preferences for male facial masculinity are not condition-dependent in a large online study,” *The All Results Journal Biology*, vol. 10, no. 1, pp. 1–6, 2018.
- [43] N. Sarkalkan, H. Weinans, and A. Zadpoor, “Statistical shape and appearance models of bones,” *Bone*, no. 60, pp. 129–140, 2014.
- [44] T. Cootes, C. Taylor, *et al.*, “Active shape models - their training and application,” *Computer Vision and Image Understanding*, vol. 61, no. 1, pp. 38–59, 1995.
- [45] T. Cootes, C. Taylor, and G. Edwards, “Active appearance models,” *IEEE Transactions On Pattern Analysis And Machine Intelligence*, vol. 23, no. 6, pp. 681–685, 2001.
- [46] M. Benjelloun, S. Mahmoudi, and F. Lecron, “A Framework of Vertebra Segmentation Using the Active Shape Model-Based Approach,” *International Journal of Biomedical Imaging*, 2011.
- [47] K. Rajmani, M. Styner, H. Talib, *et al.*, “Statistical deformable models for robust 3D surface extrapolation from sparse data,” *Medical Image Analysis*, vol. 11, pp. 99–109, 2007.
- [48] H. Thodberg and A. Roshholm, “Application of the active shape model in a commercial medical device for bone densitometry,” *Image and Vision Computing*, vol. 21, pp. 1155–1161, 2003.
- [49] C. Fitzpatrick, M. Baldwin, P. Laz, *et al.*, “Development of a statistical shape model of the patellofemoral joint for investigating relationships between shape and function,” *Journal of Biomechanics*, vol. 44, pp. 2446–2452, 2011.
- [50] T. Heap and D. Hogg, “Extending the Point Distribution Model using polar coordinates,” *Image and Vision Computing*, vol. 14, pp. 589–599, 1996.

- [51] S. Balestra, S. Schumann, J. Heverhagen, *et al.*, “Articulated Statistical Shape Model-Based 2D-3D Reconstruction of a Hip Joint,” in *Information Processing in Computer-Assisted Interventions*, pp. 128–137, Springer International Publishing, 2014.
- [52] D. Kainmueller, H. Lamecker, S. Zachow, and H. Hege, “An articulated statistical shape model for accurate hip joint segmentation,” in *2009 Annual International Conference of the IEEE Engineering in Medicine and Biology Society*, pp. 6345–6351, 2009.
- [53] R. Davies, C. Twining, and C. Taylor, *Statistical Models of Shape: Optimisation and Evaluation*, ch. Statistical Models of Shape and Appearance, pp. 9–45. Springer-Verlag London, 2008.
- [54] A. Lorusso, D. Eggbert, and R. Fisher, “Estimating 3-D rigid body transformations: a comparison of four major algorithms,” *Machine Vision and Applications*, vol. 9, pp. 272–290, 1997.
- [55] J. Gower, “Generalized Procrustes Analysis,” *Psychometrika*, vol. 40, no. 1, pp. 33–51, 1975.
- [56] L. Humbert, Y. Martelli, *et al.*, “3D-DXA: Assessing the Femoral Shape, the Trabecular Macrostructure and the Cortex in 3D from DXA images,” *IEEE Transactions On Medical Imaging*, vol. 36, no. 1, pp. 27–39, 2017.
- [57] S. Umeyama, “Least-Squares Estimation of Transformation Parameters Between Two Point Patterns,” *IEEE Transactions On Pattern Analysis And Machine Intelligence*, vol. 13, no. 4, pp. 376–380, 1991.
- [58] M. Lüthi, T. Gerig, *et al.*, “Gaussian process morphable models,” *IEEE Transactions On Pattern Analysis And Machine Intelligence*, vol. 40, no. 8, pp. 1860–1873, 2018.
- [59] P. Besl and N. McKay, “A method for registration of 3-d shapes,” *IEEE Transactions on Pattern Analysis and Machine Intelligence*, vol. 14, no. 2, pp. 239–256, 1992.
- [60] F. Vos, P. de Bruin, *et al.*, “A statistical shape model without using landmarks,” in *Proceedings of the 17th International Conference on Pattern Recognition*, vol. 3, pp. 714–717, IEEE, 2004.
- [61] T. Cootes and C. Taylor, “Statistical Models of Appearance for Computer Vision,” tech. rep., Imaging Science and Biomedical Engineering, University of Manchester, 2004.
- [62] C. Lindner, *Statistical shape and Deformation Analysis: Methods, Implementation, and Applications*, ch. Automated Image Interpretation Using Statistical Shape Models, pp. 3–32. Academic Press, 2017.
- [63] G. Tam, C. Z., and Y. o. Lai, “Registration of 3D Point Clouds and Meshes: A Survey From Rigid to Non-Rigid,” *IEEE Transactions On Visualization And Computer Graphics*, vol. 19, no. 7, 2013.
- [64] R. Davies, C. Twining, T. Cootes, J. Waterton, and C. Taylor, “3D Statistical Shape Models Using Direct Optimisation of Description Length,” in *European conference on Computer Vision*, pp. 3–20, 2002.
- [65] H. Thodberg, “Minimum Description Length Shape and Appearance Models,” in *Biennial International Conference on Information Processing in Medical Imaging*, pp. 51–62, 2003.
- [66] G. Heitz, T. Rohlfing, *et al.*, “Statistical shape model generation using nonrigid deformation of a template mesh,” in *Medical Imaging 2005: Image Processing* (J. M. Fitzpatrick and J. M. Reinhardt, eds.), vol. 5747, pp. 1411 – 1421, International Society for Optics and Photonics, SPIE, 2005.
- [67] M. Baldwin, J. Langenderfer, P. Rullkoetter, and P. Laz, “Development of subject-specific and statistical shape models of the knee using an efficient segmentation and mesh-morphing approach,” *Computer Methods And Programs in Biomedicine*, vol. 97, pp. 232–240, 2010.
- [68] E. Audenaert, J. Houcke, D. Almeida, *et al.*, “Cascaded statistical shape model based segmentation of the full lower limb in CT,” *Computer Methods In Biomechanics And Biomedical Engineering*, vol. 22, no. 6, 2019.
- [69] V. Chandran, G. Maquer, T. Gerig, P. Zysset, and M. Reyes, “Supervised learning for bone shape and cortical thickness estimation from CT images for finite element analysis,” *Medical Image Analysis*, vol. 52, pp. 42–55, 2019.
- [70] D. Madsen, A. Morel-Forster, *et al.*, “A Closest Point Proposal for MCMC-based Probabilistic Surface Registration,” *arXiv*, 2019.
- [71] D. Nolte and A. Bull, “Femur finite element model instantiation from partial anatomies using statistical shape and appearance models,” *Medical Engineering and Physics*, 2019. Article in Press.
- [72] J. Cates, S. Elhabian, and R. Whitaker, *ShapeWorks: Particle-Based Shape Correspondence and Visualization Software*, ch. 10, pp. 257 – 298. Academic Press, 2017.
- [73] M. Harris, M. Datar, R. Whitaker, *et al.*, “Statistical Shape Modelling of Cam Femoroacetabular Impingement,” *Journal of Orthopaedic Research*, pp. 1620–1626, 2013.

- [74] P. Atkins, S. Elhabian, P. Agrawal, *et al.*, “Quantitative Comparison of Cortical Bone Thickness Using Correspondence-Based Shape Modeling in Patients With Cam Femoroacetabular Impingement,” *Journal of Orthopaedic Research*, pp. 1743–1753, 2017.
- [75] B. Gaffney, T. Hillen, and J. Nepple, “Statistical Shape Modeling of Femur Shape Variability in Female Patients with Hip Dysplasia,” *Journal of Orthopaedic Research*, 2019.
- [76] A. Cheung, J. Adachi, D. Hanley, *et al.*, “High-Resolution Peripheral Quantitative Computed Tomography for the Assessment of Bone Strength and Structure: A Review by the Canadian Bone Strength Working Group,” *Current Osteoporosis Reports*, vol. 11, pp. 136–146, 2013.
- [77] I. Jolliffe, *Principal component analysis*. Springer, 1986.
- [78] C. Goodall, “Procrustes Methods in the Statistical Analysis of Shape,” *Journal of the Royal Statistical Society. Series B(Methodological)*, vol. 53, no. 2, pp. 285–339, 1991.
- [79] M. Beek, C. Small, R. Ellis, *et al.*, “Bone Alignment Using the Iterative Closest Point Algorithm,” *Journal of Applied Biomechanics*, vol. 26, pp. 526–530, 2010.
- [80] University of Basel. <https://www.futurelearn.com/courses/statistical-shape-modelling>, 2017.
- [81] M. Atallah, “A Linerar Time Algorithm For The Huasdorff Distance Between Convex Polygons,” *Information Processing Letters*, vol. 17, no. 4, pp. 207–209, 1983.
- [82] J. Fouefack, “Geometric morphometrics for 3D dense surface correspondence: Population comparisons of shoulder bone morphology,” Master’s thesis, University of Cape Town, 2018.
- [83] E. Audenaert, C. Pattyn, G. Steenackers, *et al.*, “Statistical Shape Modeling of Skeletal Anatomy for Sex Discrimination: Their Training Size, Sexual Dimorphism, and Asymmetry,” *Frontiers in Bioengineering and Biotechnology*, vol. 7, p. 302, 2019.
- [84] T. Cootes, G. Edwards, and C. Taylor, “Active appearance models,” in *European Conference on Computer Vision*, vol. 2, pp. 484–498, Springer, 1998.
- [85] H. Gray, *Anatomy of the Human Body*. Philadelphia: Lea and Febiger, 1918. [www.bartleby.com/107/](http://www.bartleby.com/107/).

## 8. Appendix

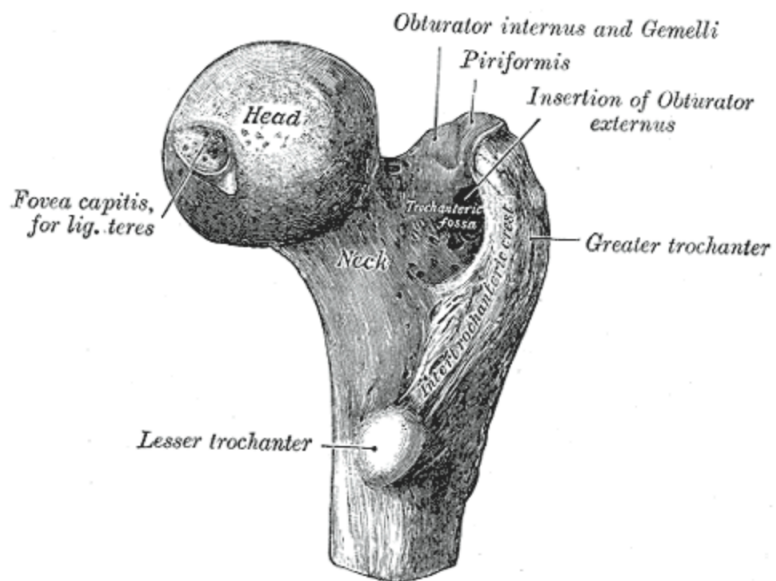


Figure 21: Illustration of a femoral head [85]